Defects in semipolar $(11\bar{2}\bar{2})$ ZnO grown on (112) $LaAlO_3$/(La,Sr)(Al,Ta)O_3 substrate by pulsed laser deposition

2013 J. Phys.: Condens. Matter 25 125801

(http://iopscience.iop.org/0953-8984/25/12/125801)

J. Phys.: Condens. Matter **25** (2013) 125801 (7pp) doi:10.1088/0953-8984/25/12/125801

Defects in semipolar $(11\bar{2}\bar{2})$ ZnO grown on (112) $LaAlO_3$/(La, Sr)(Al, Ta)O_3 substrate by pulsed laser deposition

Jr-Sheng Tian, Yue-Han Wu, Chun-Yen Peng, Kun-An Chiu, Yi-Sen Shih, Hien Do, Pei-Yin Lin, Yen-Teng Ho, Ying-Hao Chu and Li Chang

Department of Materials Science and Engineering, National Chiao Tung University, Hsinch, 300, Taiwan

E-mail: lichang@cc.nctu.edu.tw

Received 7 November 2012, in final form 24 January 2013
Published 28 February 2013
Online at stacks.iop.org/JPhysCM/25/125801

Abstract

The microstructure of semipolar $(11\bar{2}\bar{2})$ ZnO deposited on (112) $LaAlO_3$/(La, Sr)(Al, Ta)O_3 was investigated by transmission electron microscopy. The ZnO shows an in-plane epitaxial relationship of $[11\bar{2}3]_{ZnO} \parallel [11\bar{1}]_{LAO/LSAT}$ with oxygen-face sense polarity. The misfit strain along $[11\bar{2}3]_{ZnO}$ and $[1\bar{1}00]_{ZnO}$ is relieved through the formation of misfit dislocations with the Burgers vectors $\mathbf{b} = 1/6[11\bar{2}3]_{ZnO}$ and $\mathbf{b} = 1/3\langle 1\bar{2}10\rangle_{ZnO}$, respectively. The line defects in the semipolar ZnO are predominantly perfect dislocations, and the dislocation density decreases with increasing ZnO thickness as a result of dislocation reactions. Planar defects were observed to lie in the M-plane and extend along $\langle 0001\rangle$, whereas basal stacking faults were rarely found.

(Some figures may appear in colour only in the online journal)

1. Introduction

ZnO has a wide direct band gap (3.37 eV at room temperature) with large exciton binding energy (60 meV), making it a promising material for applications in high efficiency ultraviolet optoelectronic devices. As a wurtzite form with space group $P6_3mc$, ZnO lacks an inversion center, and forms a strong asymmetry along $\langle 0001\rangle$. For a quantum well (QW) structure built in the conventional (0001) growth direction, the asymmetry will cause discontinuous polarization at the interfaces of the QWs, therefore resulting in the so-called quantum-confined Stark effect (QCSE) which decreases the luminous efficiency [1]. To avoid this problem, ZnO is intentionally grown in the nonpolar planes where the *c*-axis lies, and no polarization discontinuities will arise at the interfaces.

Recent research has shown that nonpolar ZnO can be successfully deposited on various substrates, such as R-plane sapphire, (100) $LiAlO_2$, (100) $SrTiO_3$ and $LaAlO_3$, and (112) $LaAlO_3$ (LAO) [2–5]. However, high density basal stacking faults (BSFs) and threading dislocations (TDs) are often observed in such nonpolar films [6, 7]. These defects are usually generated during initial growth by biaxial misfit stresses and by the coalescence of adjacent islands which are misoriented with respect to one another, and are believed to degrade the performance of luminescent devices [6, 8]. Up to now, the reduction of defect density for achieving high quality nonpolar ZnO films has remained a challenge.

Alternatively, growth of semipolar ZnO is another approach for reducing the QCSE. It has been reported that discontinuous polarization in semipolar III nitride can be effectively reduced [9]. Recently, we have obtained semipolar $(11\bar{2}\bar{2})$ ZnO on (112) $(LaAlO_3)_{0.29}(Sr_2AlTaO_6)_{0.35}$ (LSAT, cubic perovskite with $a = 3.868$ Å) substrates with LAO buffer layers (bulk LAO is a pseudo-cubic perovskite with $a = 3.791$ Å) by pulsed laser deposition (PLD) [10]. The growth of semipolar ZnO has been characterized as single-domain epitaxy, and the film has a reducing dislocation density with increasing ZnO layer thickness. Thus, it is possible to achieve high quality heteroepitaxial $(11\bar{2}\bar{2})$ ZnO films. Nevertheless, the defect structure and the reduction mechanism in the semipolar ZnO films are still not clear. In this study, we employ transmission electron microscopy (TEM) to investigate the microstructure of $(11\bar{2}\bar{2})$ ZnO, and the reduction of the defect density is discussed.

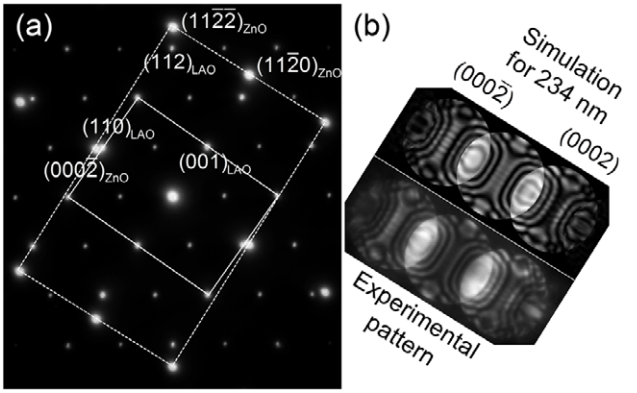

Figure 1. (a) XTEM selected-area diffraction pattern acquired from the region of the ZnO/LAO interface along $[1\bar{1}00]_{ZnO}/[1\bar{1}0]_{LAO}$ on LSAT. The dotted line and solid line indicate the diffraction patterns of ZnO and LAO/LSAT, respectively. (b) Simulated and experimental CBED patterns of ZnO along the zone axis of $[1\bar{1}00]_{ZnO}$.

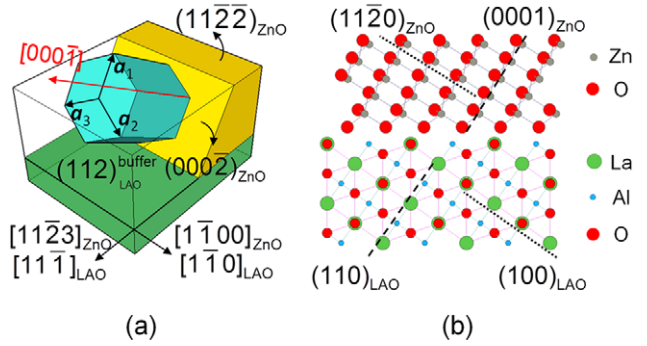

Figure 2. (a) The epitaxial relationship between semipolar $(11\bar{2}\bar{2})$ ZnO and (112) LAO buffer. A display of $\boldsymbol{a}_1$-, $\boldsymbol{a}_2$-, and $\boldsymbol{a}_3$-vectors in $(11\bar{2}\bar{2})$ ZnO. (b) Atomic configuration of $(11\bar{2}\bar{2})$ ZnO and LAO buffer on the zone axis of $[1\bar{1}00]_{ZnO}/[1\bar{1}0]_{LAO}$. The large and small spheres in ZnO represent oxygen and Zn atoms, respectively. In LAO, the atoms from large to small are La, oxygen, and Al atoms, respectively.

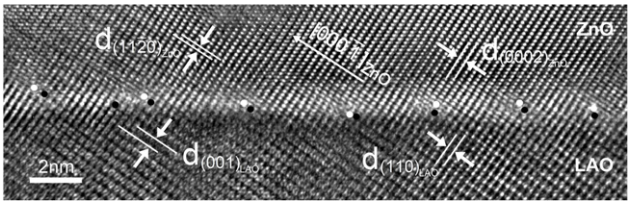

Figure 3. (a) Cross-sectional high resolution TEM images at the ZnO/LAO interface along the zone axis of $[1\bar{1}00]_{ZnO}/[1\bar{1}0]_{LAO}$. The black and white circles indicate the relative locations of MDs with $\mathbf{b} = 1/6[11\bar{2}0]_{ZnO}$ and $\mathbf{b} = 1/2[0001]_{ZnO}$, respectively.

2. Experimental details

The processes of growth of ZnO and LAO buffer were carried out by using PLD in oxygen ambient. Before deposition, (112) LSAT substrate was thermally cleaned at 850 °C in vacuum for 30 min in the PLD chamber. After the cleaning, 100 nm of LAO buffer was grown on LSAT substrate at 750 °C in 0.14 mTorr; then the LAO/LSAT was annealed at 850 °C in 100 mTorr for 1 h. Further 200 nm and 1.6 μm ZnO films were deposited at 750 °C and 50 mTorr with the growth rate of 200 nm h^{-1}. Here, we used the annealed LAO buffer because it, unlike (112) bulk LAO, can provide a suitable surface for semipolar $(11\bar{2}\bar{2})$ ZnO growth rather than for nonpolar $(10\bar{1}0)$ ZnO growth [5]. Besides, the LAO buffer is fully strained on LSAT substrate and is free of transformed twins which commonly exist in bulk LAO. As a result, no phase transformation occurs in the LAO buffer during cooling, and the above ZnO film is not distorted [10–12].

We used high resolution TEM (HRTEM) to inspect the interface structure of 200 nm ZnO along $[1\bar{1}00]_{ZnO}$ and $[11\bar{2}3]_{ZnO}$ by employing a JEOL ARM 200F TEM microscope. HRTEM filtering was applied to HRTEM images to remove background. The defect structure of semipolar ZnO was investigated on a 1.6 μm ZnO film along the zone axes of $[1\bar{1}00]_{ZnO}$ and $[11\bar{2}3]_{ZnO}$ by using JEOL JEM-2010 and JEM-2100 TEM microscopes. Cross-sectional TEM (XTEM) foils were prepared by using a focused ion beam (FIB) of 30 keV Ga^+ ion energy with Pt-protective coating.

3. Results and discussion

3.1. The epitaxial relationship and misfit dislocations

Figure 1(a) is a selected-area diffraction pattern obtained from the region of the ZnO/LAO interface, showing the epitaxial relationship of $(11\bar{2}\bar{2})_{ZnO} \parallel (112)_{LAO}$ and $[1\bar{1}00]_{ZnO} \parallel [1\bar{1}0]_{LAO}$. The polarization of ZnO was determined by using convergent beam electron diffraction (CBED). In the CBED patterns shown in figure 1(b), along $[1\bar{1}00]_{ZnO}$, we can distinguish the contrast between (0002) and $(000\bar{2})$ disks by comparing with simulation patterns of 234 nm foil thickness (using MacTempas® simulation software). This reveals that the semipolar ZnO is grown with oxygen-face sense polarity, which means that the polar axis $[000\bar{1}]_{ZnO}$ direction points to the surface with an inclination angle, and therefore the $(11\bar{2}\bar{2})$ index is adopted as the notation for this [13]. According to the results, both the epitaxial relationship of ZnO on LAO buffers and the atomic configuration on the zone axis of $[1\bar{1}00]_{ZnO}$ can be illustrated as shown in figures 2(a) and (b), respectively. Thus, the lattice misfit between $(11\bar{2}\bar{2})$ ZnO and (112) LAO buffer is calculated as -2.93% and $+8.39\%$ along $[1\bar{1}00]_{ZnO}$ and $[11\bar{2}3]_{ZnO}$, respectively [10].

Figure 3 shows HRTEM images at the interfacial region of $(11\bar{2}\bar{2})$ ZnO/LAO on the zone axis of $[1\bar{1}00]_{ZnO}$. It is clearly seen that the $(0002)_{ZnO}$ lattice fringes are nearly parallel to $(110)_{LAO}$ ones, and $(11\bar{2}0)_{ZnO}$ fringes are also nearly parallel to $(001)_{LAO}$ ones. This confirms the epitaxial relationship of figure 2(b). To characterize the relaxation of misfit strain in the heteroepitaxial $(11\bar{2}\bar{2})$ ZnO, we first inspect the Burgers vector of misfit dislocations (MDs) by utilizing Burgers circuits. As shown in figure 4(a), two white dots represent the start and the end of the Burgers circuit. This clearly reveals that the three Burgers circuits show the same displacement with Burgers vector $\mathbf{b} = 1/6[11\bar{2}3]_{ZnO}$. The vector of $1/6[11\bar{2}3]_{ZnO}$ can be regarded as the combination

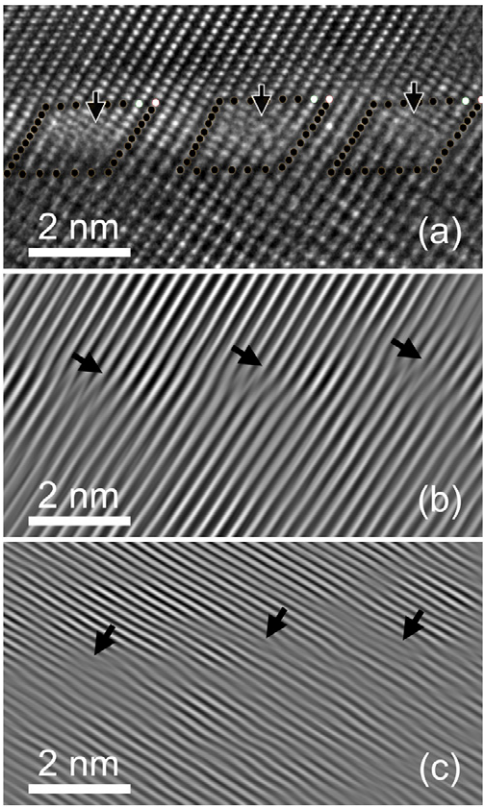

Figure 4. (a) Cross-sectional high resolution TEM image of the ZnO/LAO interface for the zone axis of $[1\bar{1}00]_{ZnO}/[1\bar{1}0]_{LAO}$. Burgers circuits reveal the misfit dislocation with $\mathbf{b} = 1/6[11\bar{2}3]$ to relax the lattice mismatch strain of ZnO on LAO buffer. (b) Fourier-filtered images of (a) using FFT $(0002)_{ZnO}$ and $(110)_{LAO}$ diffraction spots. (c) Fourier-filtered images of (a) using FFT $(11\bar{2}0)_{ZnO}$ and $(001)_{LAO}$ diffraction spots. The black arrows indicate the positions of extra half-planes in Fourier-filtered images.

of $1/6[11\bar{2}0]_{ZnO}$ and $1/2[0001]_{ZnO}$, which correspond to the *d*-spacings of $(11\bar{2}0)_{ZnO}$ and $(0002)_{ZnO}$, respectively. As shown in figures 4(b) and (c), extra $(0002)_{ZnO}$ and $(11\bar{2}0)_{ZnO}$ half-planes near the MDs are clearly observed in the Fourier-filtered images formed by using $(0002)_{ZnO}/(110)_{LAO}$ and $(11\bar{2}0)_{ZnO}/(001)_{LAO}$ spots in the fast Fourier transform (FFT) pattern of figure 4(a), respectively. It is possible that these MDs are geometrical dislocations and are generated at the beginning of growth in one or two monolayers due to a large lattice misfit +8.39% resulting in small critical relaxation thickness. The relaxation process is similar to the domain matching epitaxy proposed by Narayan *et al* [14], and will not introduce TDs. If the MDs were generated by a glide process, high energy prismatic $(11\bar{2}0)$ and basal stacking faults bounded by partial TDs would form due to the Burgers vectors $\mathbf{b} = 1/2[0001]$ and $1/6[11\bar{2}0]$ not being lattice translation vectors. Therefore, the glide relaxation process is energetically unfavorable. Actually, we do not observe such stacking faults in TEM images under two-beam conditions.

For semipolar $(11\bar{2}2)$ III nitride/GaN, the misfit strain along $[11\bar{2}3]$ is relaxed by forming MDs through $(0001)/[11\bar{2}0]$ glide systems, and the MDs with $\mathbf{b} = 1/3[11\bar{2}0]$ cause mismatch-dependent lattice tilting of III nitride with respect to GaN substrate along $[11\bar{2}3]$ [15]. In our case, either extra half-plane, $(0002)_{ZnO}$ or $(11\bar{2}0)_{ZnO}$, will cause lattice tilting, but no tilting will occur when they become a pair, such as the MDs observed in figure 4(a). Nevertheless, in the 200 nm thick $(11\bar{2}2)$ ZnO film, a slight lattice tilting of 0.129° along $[11\bar{2}3]$ was detected from x-ray rocking curves (not shown here), and the tilt direction may be related to the existence of extra $(11\bar{2}0)_{ZnO}$ MDs with **b** parallel to $1/3[11\bar{2}0]$.

In figure 3, we labeled the relative locations of MDs with $\mathbf{b} = 1/6[11\bar{2}0]_{ZnO}$ and $\mathbf{b} = 1/2[0001]_{ZnO}$ by black and white circles, respectively. It is shown that there are eight $(11\bar{2}0)_{ZnO}$ extra half-planes and seven $(0002)_{ZnO}$ extra half-planes in the region. Therefore, the additional $(11\bar{2}0)_{ZnO}$ extra half-plane with $\mathbf{b} = 1/6[11\bar{2}0]_{ZnO}$ can result in lattice tilting in the semipolar ZnO. It is also found that the average spacing of $(0002)_{ZnO}$ extra half-planes is $11.83 \times d_{(0002)}$, and the average spacing of $(11\bar{2}0)_{ZnO}$ extra half-planes is $10.3 \times d_{(11\bar{2}0)}$. For full relaxation along $[11\bar{2}3]_{ZnO}$ of $(11\bar{2}2)$ ZnO with slight tilting on fully strained LAO buffer, one extra half-plane will be found in $N \cong 12$ planes according to the equation $N = d_{[11\bar{1}]LAO}/(d_{[11\bar{1}]LAO} - d_{[11\bar{2}3]ZnO})$. The average value from the region examined in figure 3 is close to $N \cong 12$, indicating that the misfit strain along $[11\bar{2}3]_{ZnO}$ is almost fully relaxed in the 200 nm semipolar ZnO.

Relaxation of misfit strains along $[1\bar{1}00]_{ZnO}$ is investigated by using HRTEM with the zone axis of $[11\bar{2}3]_{ZnO}$ as shown in figure 5(a). Figure 5(b) shows the FFT pattern of figure 5(a) representing the lattice relationship of ZnO/LAO. It is found that only one MD is observed in the 14 nm wide region of figure 5(a). This is due to the small lattice mismatch $\sim -2.93\%$ along $[1\bar{1}00]_{ZnO}$ which would result in an MD array with average spacing of 9.6 nm in fully relaxed conditions. The Burgers circuit around the MD shows a displacement which is coincident with the projective component of the lattice vector $\boldsymbol{a}_2$ (or $\boldsymbol{a}_3$) along $[11\bar{2}3]_{ZnO}$. Therefore, the MD is mixed type and has a line direction along $[11\bar{2}3]_{ZnO}$ with $\mathbf{b} = \boldsymbol{a}_2$ (or $\boldsymbol{a}_3$), and its edge component corresponds to $(1\bar{1}0)_{LAO}$ and $(0\bar{1}\bar{1})_{LAO}$ extra half-planes as shown in the Fourier-filtered images in figures 5(c) and (d) by using $(1\bar{1}00)_{ZnO}/(1\bar{1}0)_{LAO}$ and $(0\bar{1}11)_{ZnO}/(0\bar{1}\bar{1})_{LAO}$ spots in the FFT pattern of figure 5(b), respectively.

The MDs relieving misfit strain along $[1\bar{1}00]$ show a line direction along $[11\bar{2}3]$ with $\mathbf{b} = 1/3[1\bar{2}10]$. There are two ways of generating the MDs. Since the $(11\bar{2}2)$ ZnO shows an island growth mode at the initial growth stage as evidenced from spot patterns of *in situ* reflection high energy electron diffraction (RHEED) (not shown here), geometrical MDs can be introduced at the edge of growing islands and will not produce TDs [16, 17]. The other model is based on the glide mechanism; as shown in figure 5(e), dislocations nucleating at the surface can glide to the interface through non-basal slip systems $\{\bar{1}011\}/\langle 1\bar{2}10\rangle$ ($(\bar{1}011)/[1\bar{2}10]$ and $(0\bar{1}11)/[\bar{2}110]$), for which MDs will be formed with the line direction along $[11\bar{2}3]$ and $\mathbf{b} = 1/3[1\bar{2}10]$. To examine that possibility, the Schmidt factor for misfit stress along $[1\bar{1}00]$ on $\{\bar{1}011\}/\langle 1\bar{2}10\rangle$ is calculated, and the value is 0.3809. Thus, the glide of $\{\bar{1}011\}/\langle 1\bar{2}10\rangle$ can be driven by the misfit stress. Moreover, the small lattice mismatch (-2.93%) along

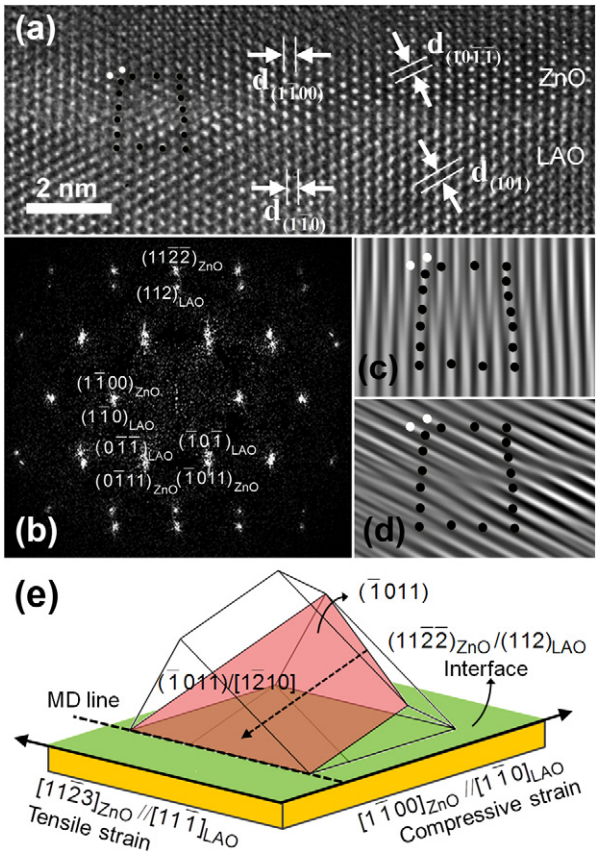

Figure 5. (a) Cross-sectional high resolution TEM image of the ZnO/LAO interface for the zone axis of $[11\bar{2}3]_{ZnO}/[11\bar{1}]_{LAO}$. Two white dots represent the start and the end of the Burgers circuit. (b) FFT pattern of (a). (c) Fourier-filtered images using FFT $(1\bar{1}00)_{ZnO}$ and $(1\bar{1}0)_{LAO}$ diffraction spots. (d) Fourier-filtered images using FFT $(0\bar{1}11)_{ZnO}$ and $(0\bar{1}\bar{1})_{LAO}$ diffraction spots. (e) Possible mechanism for relieving misfit strain along $[1\bar{1}00]_{ZnO}$ by generating MDs through $\{\bar{1}011\}/\langle 1\bar{2}10\rangle$ glide systems.

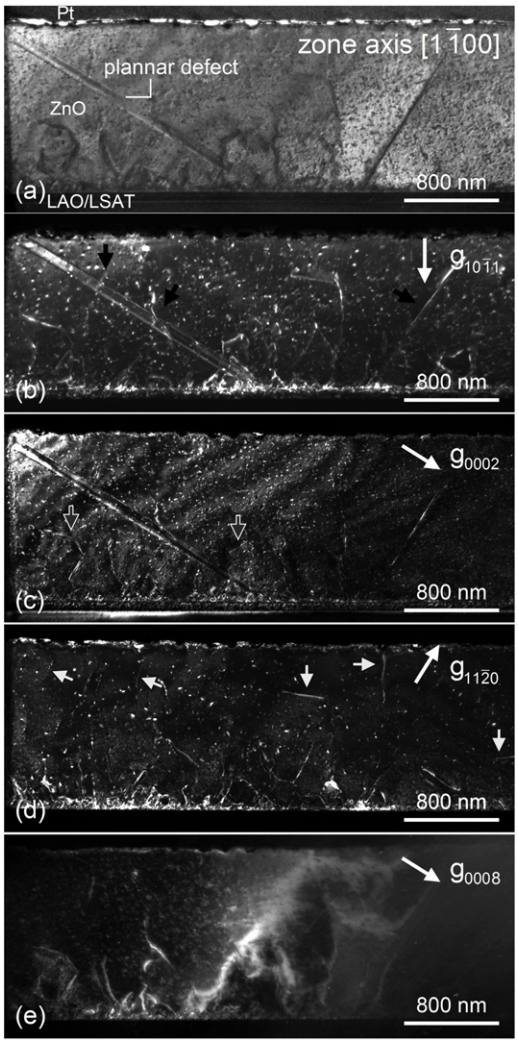

Figure 6. (a) XTEM bright-field image along the zone axis of $[1\bar{1}00]$. ((b)–(d)) Weak-beam dark-field images near the $[1\bar{1}00]$ zone axis with $\mathbf{g} = 10\bar{1}1$, $\mathbf{g} = 0002$, and $\mathbf{g} = 11\bar{2}0$, respectively. The arrows in (b)–(d) indicate the $(\boldsymbol{a}+\boldsymbol{c})$-type, $\boldsymbol{c}$-type and $\boldsymbol{a}$-type dislocations, respectively. (e) A dark-field image near the [100] zone axis with $\mathbf{g} = 0008$.

$[1\bar{1}00]_{ZnO}/[1\bar{1}0]_{LAO}$ and the small surface energy of $\{\bar{1}011\}$ are also favorable for the glide process [18].

Misfit strain relaxation through gliding on non-basal planes in semipolar wurtzite III nitrides has recently been reported by Wu *et al* and Hardy *et al* [19, 20]. For $(11\bar{2}2)$ InGaN grown on GaN substrate, the compressive misfit strain in InGaN $[1\bar{1}00]$ can be relaxed through the MDs generated by gliding from the non-basal slip systems $\{10\bar{1}0\}/\langle 1\bar{2}10\rangle$. The MDs from $\{10\bar{1}0\}/\langle 1\bar{2}10\rangle$ are also responsible for relieving the $[11\bar{2}\bar{3}]$ misfit compressive strain due to the MD line direction $\langle\bar{2}4\bar{2}\bar{3}\rangle$ being inclined to both $[11\bar{2}\bar{3}]$ and $[1\bar{1}00]$ directions. However, in our case, if the MDs relieving compressive strain along $[1\bar{1}00]$ were generated from gliding of $\{10\bar{1}0\}/\langle 1\bar{2}10\rangle$, it would introduce additional tensile strain along $[11\bar{2}3]$ which is initially under tensile strain +8.39%. Therefore, the mechanism of gliding through slip systems $\{10\bar{1}0\}/\langle 1\bar{2}10\rangle$ may not be favorable for relaxing the misfit strain of $(11\bar{2}\bar{2})$ ZnO grown on (112) LAO/LSAT.

3.2. Defect characterization and the TD reduction mechanism

In order to inspect the characteristics of defects in semipolar $(11\bar{2}\bar{2})$ ZnO, XTEM observations were performed on a 1.6 μm thick ZnO layer under various two-beam conditions. Figures 6 and 7 show XTEM images observed along zone axes of $[1\bar{1}00]$ and $[11\bar{2}3]$, respectively, under several different two-beam conditions for the same examined region. In each image, the layers in the order from top to bottom are Pt-protective coating, ZnO layer, LAO buffer, and LSAT substrate.

As seen in figure 6(a), there is a planar defect which features as a boundary extending along $\langle 0001\rangle$ from near the interface through the whole ZnO layer to the surface. The Burgers vector of the planar defect is analyzed by using the two-beam condition according to the invisibility criterion $\mathbf{g}\cdot\mathbf{b} = n$, where n is an integer. In dark-field images of figure 6, the contrast of the planar defect appears with $\mathbf{g} = 10\bar{1}1$ and $\mathbf{g} = 0002$, but no contrast for $\mathbf{g} = 11\bar{2}0$ and $\mathbf{g} = 0008$. This suggests that the displacement of the lattice across the defect boundary has only a $\langle 000w\rangle$

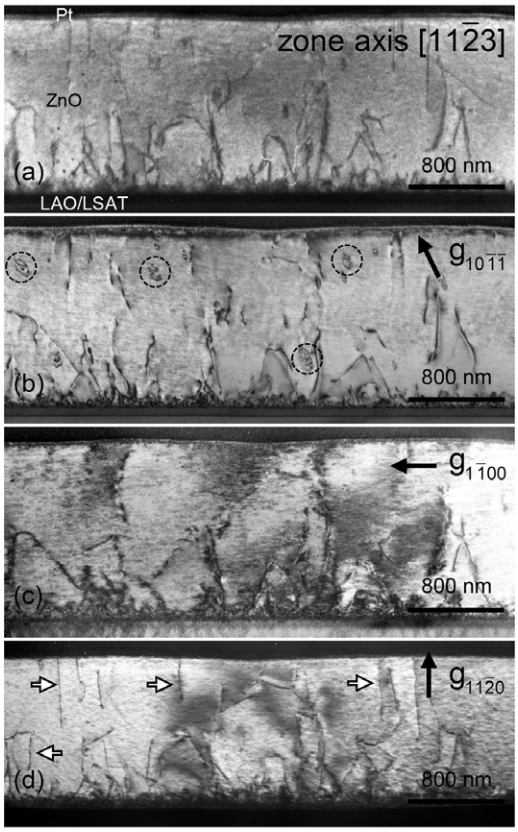

Figure 7. (a) XTEM bright-field image along the zone axis of [11$\bar{2}$3]. ((b), (c)) Bright-field images near the [11$\bar{2}$3] zone axis with $\mathbf{g} = 10\bar{1}1$ and $\mathbf{g} = 1\bar{1}00$, respectively. Planar defects are indicated by dashed circles. (d) Bright-field image taken with $\mathbf{g} = 11\bar{2}0$ near the zone axis of [0001] after tilting the sample by about 30°.

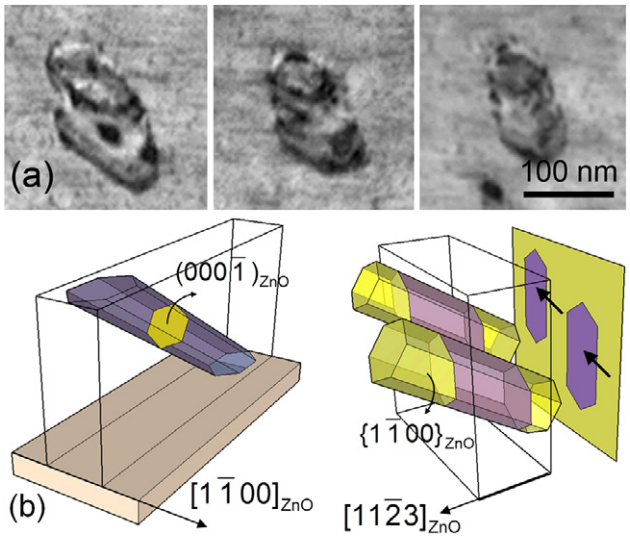

Figure 8. (a) Enlargements of the planar defects in figure 7(b). (b) Perspective illustration of the planar defects intersecting XTEM foils along the zone axes of $[1\bar{1}00]_{ZnO}$ and $[11\bar{2}3]_{ZnO}$. The arrows indicate the projection of planar defects from the XTEM foils along the $[11\bar{2}3]_{ZnO}$ zone axis.

component with $w \neq 1/2$ and $w = n/8$. Observing the [11$\bar{2}$3] cross-section, apparent fringe contrast can be observed in many regions, as indicated by dashed circles in figure 7(b) for $\mathbf{g} = 10\bar{1}1$, but it disappears for $\mathbf{g} = 1\bar{1}00$ and $\mathbf{g} = 11\bar{2}0$. This indicates that there are planar defects overlapping with the ZnO matrix in the regions with displacement only of the ⟨0001⟩ component. In figure 8(a), the enlargement of the fringe contrast is clearly shown to be surrounded by $\{10\bar{1}0\}$ boundaries and they exhibit hexagon-like shape with size about 100 nm, which is approximately the width of the planar defect in figure 6. Therefore, we can deduce that the extended planar defects in figure 6 actually have the shape of a ⟨0001⟩-oriented hexagonal column bounded with $\{10\bar{1}0\}$, with displacement ⟨000w⟩ from the ZnO matrix, and the appearance of the fringe contrast in figure 7(b) is due to the oblique intersection of the hexagonal column of ZnO with the foil. The hexagonal column planar defect intersecting the XTEM foil with the zone axes $[1\bar{1}00]_{ZnO}$ and $[11\bar{2}3]_{ZnO}$ is illustrated in figure 8(b), and the foil is shown as a transparent rectangular solid. The planar defect in our case is similar to the inversion domain boundary (IDB) of wurtzite GaN which also has the form of a ⟨0001⟩-oriented hexagonal column bounded by prismatic $\{10\bar{1}0\}$ boundaries, and extends through the whole epilayer [21]. Likewise, the IDB in GaN is out of contrast in the TEM two-beam images with excitation of (hki0) [21, 22]. Theoretical study of the IDB in ZnO shows structure similar to that of the IDB in GaN, where the lattice across the IDB has interchanged cation and anion sites with 1/2[0001] displacement. Therefore, the shift of the lattice point across the IDB is about ∼1/8[0001], and results in contrast with excitation of ($hkil$) with $l \neq 0$ and $l \neq 8$ [23]. In figure 6(e), the contrast of planar defects has disappeared in the dark-field images with $\mathbf{g} = 0008$, suggesting that the defects are probably IDB ones.

Except for the ⟨0001⟩-oriented defects, BSFs, the most commonly observed planar defects in nonpolar ZnO, are hard to observe by comparing all our examined two-beam images over a range around 3 μm width for the semipolar ZnO. As shown in figure 6, a few defects lying in the basal plane are observed in the region above 200 nm from the interface, and these defects are in contrast under $\mathbf{g} = 0002$ conditions. For I_1, I_2, and extrinsic BSFs, they are all invisible under $\mathbf{g} = 0002$; therefore, these defects in the basal plane are perfect dislocations [6]. The absence of BSFs in the observed regions is explained by the low density in the semipolar ZnO film. This is confirmed by using low temperature photoluminescence and a Williamson–Hall plot of $\{h0\bar{h}0\}$ x-ray rocking curves, and the density is estimated to be about 1×10^4 cm^{-1} which is consistent with the TEM observations [8, 10, 24].

For nonpolar and semipolar wurtzite heteroepitaxial films, the BSF density is usually in the range of 10^5–10^6 cm^{-1}. The origin of the stacking faults in nonpolar ZnO has been studied by Vennéguès *et al* [25]. They found that the main mechanism of formation of stacking faults is a compensation for the translation between neighboring islands during coalescence. The translation is produced after the geometrical misfit dislocations are independently introduced in every grown island (the Volmer–Weber growth mode).

Besides, it is also the case that the density of BSFs resulting from the mechanism will decrease from nonpolar to polar orientation due to the decreasing ability of stacking faults to compensate for the in-plane translation between neighboring islands, and the formation of dislocations is favorable for the compensation.

For the $(11\bar{2}\bar{2})$ ZnO, spot patterns of RHEED obtained at the initial growth stage suggest the Volmer–Weber growth mode. Therefore, it can be expected that the BSF density in the semipolar $(11\bar{2}2)$ ZnO is less than that in nonpolar ZnO if the BSFs are formed to compensate for the lattice translation during coalescence. However, the density, comparing to that in semipolar (112) GaN, is still relatively low [26, 27]. This is attributed to the formation of I_1 BSFs being more favored in GaN than in ZnO, as evidenced by the larger size of the BSFs in GaN (several hundred nanometers to microns) than in ZnO (30–200 nm) [6, 28].

Characteristics of the dislocations in the 1.6 μm ZnO are generally shown in figures 6 and 7. It is found that the dislocation density close to the interface is near the range of 10^{11}–10^{12} cm^{-2}, and decreases to about 5×10^9 cm^{-2} in the middle of the ZnO layer. For dislocations reaching the 1.6 μm ZnO surface it can be shown that the density is below 1×10^9 cm^{-2}. This indicates that the dislocations are dramatically reduced with increasing ZnO thickness. The dislocation reduction can be described using the trace of the dislocation lines, as in the observation near the interface, dislocations are initially entangled in highly defected regions, and then a few threading dislocations (TDs) propagate through the regions with various orientations. The varied line directions might be related to minimization of the total strain energy with different Burgers vectors, and would enhance the probability of dislocation reactions [29]. A universal observation from the interface to the upper layer shows that many dislocations come across each other, and therefore form half-loops or are fused into dislocations with compound Burgers vectors, which may be involved in another interaction as well. Consequently, the dislocation density might continuously decrease with increasing ZnO thickness. For heteroepitaxial (100) GaAs films, a similar reduction has been reported [30]. Owing to the inclined and intersecting slip systems $\langle 110\rangle/\{111\}$ in (100) GaAs, the points of intersection of inclined dislocations with the surface will move towards each other as the layer thickness increases. When the points become close enough, dislocations will have reactions among themselves through glide or cross-slip in these slip planes, or climb out of the slip planes. In semipolar $(11\bar{2}\bar{2})$ ZnO, most possible slip planes, like $\{0001\}$, $\{1\bar{1}00\}$, $\{10\bar{1}1\}$ and $\{11\bar{2}2\}$, are also inclined to the surface normal and intersect each other; therefore, the TD reduction would probably result from dislocation reactions.

To confirm the dislocation reaction, we investigated another XTEM foils prepared along $[1\bar{1}00]_{\mathrm{ZnO}}$ by using the invisibility criterion $\mathbf{g} \cdot \mathbf{b} = 0$ to identify the Burgers vectors of dislocations. In figure 9, two regions which are above 1 μm from the interface are examined with two-beam conditions with $\mathbf{g} = 11\bar{2}0$ and $\mathbf{g} = 0002$. By comparing the line positions for each excitation condition, two fusion

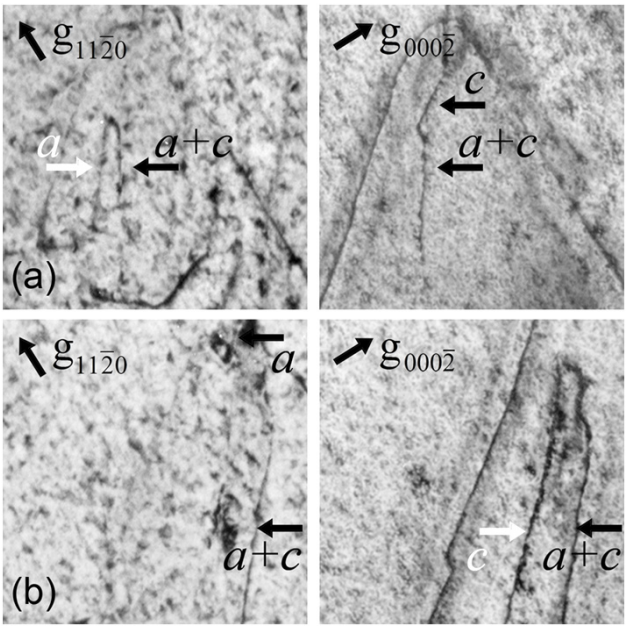

Figure 9. BF TEM images showing, in (a) and (b), the fusion reactions of $(\boldsymbol{a}+\boldsymbol{c})+(-\boldsymbol{a}) \rightarrow \boldsymbol{c}$ and $(\boldsymbol{a}+\boldsymbol{c})+(-\boldsymbol{c}) \rightarrow \boldsymbol{a}$, respectively.

reactions for dislocation reduction can be clearly identified as $(\boldsymbol{a}+\boldsymbol{c})+(-\boldsymbol{a}) \rightarrow \boldsymbol{c}$ and $(\boldsymbol{a}+\boldsymbol{c})+(-\boldsymbol{c}) \rightarrow \boldsymbol{a}$ in figures 9(a) and (b), respectively. These two reactions are also found by examination to be energetically favorable by using Frank's rule for dislocation reaction. However, the reaction of dislocations has been reported to depend on the population of dislocations [31]. Thus, we have further investigated the population of TDs in semipolar ZnO and discuss the reactions between dislocations in the following.

We inspected the Burgers vectors of dislocations in the ZnO layer by employing the invisibility criterion $\mathbf{g} \cdot \mathbf{b} = 0$ under various two-beam conditions. $(\boldsymbol{a}+\boldsymbol{c})$-type, $\boldsymbol{c}$-type, and $\boldsymbol{a}$-type dislocations are all observed in the semipolar ZnO, and most of them are mixed dislocations. Some of $(\boldsymbol{a}+\boldsymbol{c})$-type, $\boldsymbol{c}$-type, and $\boldsymbol{a}$-type dislocations are indicated by arrows in figures 6(b)–(d), respectively. In further examination of a 10 μm wide region, over one hundred dislocations are found above 200 nm from the interface. Among the observed dislocations, $\boldsymbol{a}$-type dislocations are dominant: ~67% of them, and the rest are $(\boldsymbol{a}+\boldsymbol{c})$-type and $\boldsymbol{c}$-type dislocations, between which the population ratio is near 1:1 for the non-$\boldsymbol{a}$-type dislocations. Those dislocations with the Burgers vector being an $\boldsymbol{a}$-vector can be further classified as $\boldsymbol{a} = \boldsymbol{a}_1$ or $\boldsymbol{a} = \boldsymbol{a}_2$ or $\boldsymbol{a}_3$ where the vectors $\boldsymbol{a}_1, \boldsymbol{a}_2$, and $\boldsymbol{a}_3$ in $(11\bar{2}\bar{2})$ ZnO are labeled in figure 2(a). As shown in figures 7(c) and (d), the BF image with $\mathbf{g} = 1\bar{1}00$ excludes the contrast of $\boldsymbol{a}_1$-type and $(\boldsymbol{a}_1+\boldsymbol{c})$-type dislocations, and the BF image with $\mathbf{g} = 11\bar{2}0$ shows all $\boldsymbol{a}$-type and $(\boldsymbol{a}+\boldsymbol{c})$-type dislocations. Above 200 nm from the ZnO/LAO interface, the density of dislocations having an $\boldsymbol{a}_1$-vector is similar to that of $\boldsymbol{a}_2/\boldsymbol{a}_3$-vector dislocations. As regards the dislocations near the ZnO surface in figures 6 and 7, most of them are found to be $\boldsymbol{a}$-type and $(\boldsymbol{a}+\boldsymbol{c})$-type ones, whereas pure $\boldsymbol{c}$-type dislocations

are rarely observed. Moreover, the $\boldsymbol{a}$-vector seems to be slightly dominated with $\boldsymbol{a}_1$ rather than $\boldsymbol{a}_2$ or $\boldsymbol{a}_3$, as shown in figures 7(c) and (d). Therefore, the reactions responsible for dislocation reduction may differ from near the interface to the surface of 1.6 μm ZnO due to the varied dislocation populations.

By checking the Burgers vector and the trace of the TDs in XTEM images along $[11\bar{2}3]$, it is found that the dislocations with $\mathbf{b} = \boldsymbol{a}$ or $\mathbf{b} = \boldsymbol{a} + \boldsymbol{c}$, where $\boldsymbol{a} = \boldsymbol{a}_2$ or $\boldsymbol{a}_3$, have inclined line directions, and the dislocation lines with the $\boldsymbol{a}_1$-vector are relatively straight. The inclined dislocation lines are expected to increase the probability of reaction between TDs with $\boldsymbol{a}_2$- and $\boldsymbol{a}_3$-vectors as the thickness increases [31]. This is because the inclined dislocations can propagate farther than straight dislocations as the thickness increases, so they have more opportunity to meet each other. Under this consideration, the fusion rate in $\boldsymbol{a}_2 + \boldsymbol{a}_3 \rightarrow -\boldsymbol{a}_1$ being larger than that in $\boldsymbol{a}_1 + \boldsymbol{a}_2 \rightarrow -\boldsymbol{a}_3$ accounts for there being more TDs with the $\boldsymbol{a}_1$-vector than with the $\boldsymbol{a}_2$- and $\boldsymbol{a}_3$-vectors near the surface of a thick ZnO layer. However, the straight line dislocations with the $\boldsymbol{a}_1$-vector along the zone axis of $[11\bar{2}3]$ are revealed to mainly lie along $(1\bar{1}00)$ and cannot effectively move laterally along $[1\bar{1}00]$. This would hinder the reaction between two dislocations with the $\boldsymbol{a}_1$-vector when the distance between them along $[1\bar{1}00]$ is great enough. Therefore, for a very thick ZnO layer, the reduction of TDs with an $\boldsymbol{a}_1$-vector may rely mainly on the reaction with TDs having $\boldsymbol{a}_2$- or $\boldsymbol{a}_3$-vectors.

4. Summary

We have investigated the microstructure of semipolar $(11\bar{2}\bar{2})$ ZnO on (112) LAO/LSAT and the dislocation reduction mechanisms. The semipolar ZnO shows an epitaxial relationship of $(11\bar{2}\bar{2})_{\mathrm{ZnO}} \parallel (112)_{\mathrm{LAO}}$ and $[1\bar{1}00]_{\mathrm{ZnO}} \parallel [1\bar{1}0]_{\mathrm{LAO/LSAT}}$, and exhibits oxygen-face sense polarity. The misfit strain along $[11\bar{2}3]_{\mathrm{ZnO}}$ is almost fully relaxed by forming MD pairs with Burgers vectors $\mathbf{b} = 1/6[11\bar{2}0]_{\mathrm{ZnO}}$ and $\mathbf{b} = 1/2[0001]_{\mathrm{ZnO}}$. For misfit strain relaxation along $[1\bar{1}00]_{\mathrm{ZnO}}$, mixed-type MDs with $\mathbf{b} = \boldsymbol{a}_2$ or $\boldsymbol{a}_3$ are observed on the zone axis of $[11\bar{2}3]_{\mathrm{ZnO}}$. Line and planar defects in the ZnO layer are also investigated. Planar defects in semipolar ZnO are shown as $\{10\bar{1}0\}$ boundaries with the shape of a hexagonal column extending from near the interface to the surface. Besides this, basal stacking faults in the $\sim$3 μm examined region are rarely observed, indicating that the density is low. Linear defects are predominantly perfect dislocations with $\mathbf{b} = (\boldsymbol{a} + \boldsymbol{c}), \boldsymbol{c}$, and $\boldsymbol{a}$, and the density gradually decreases with increasing ZnO thickness due to dislocation reactions.

Acknowledgment

This work was supported by the National Science Council, Taiwan, under Contract No. NSC98-2221-E-009-042-MY3.

References

[1] Waltereit P, Brandt O, Trampert A, Grahn H T, Menniger J, Ramsteiner M, Reiche M and Ploog K H 2000 *Nature* **406** 865
[2] Moriyama T and Fujita S 2005 *Japan. J. Appl. Phys.* **44** 7919
[3] Chou M C, Chang L, Chung H Y, Huang T H, Wu J J and Chen C W 2007 *J. Cryst. Growth* **308** 412
[4] Ho Y T, Wang W L, Peng C Y, Liang M H, Tian J S, Lin C W and Chang L 2008 *Appl. Phys. Lett.* **93** 121911
[5] Ho Y T, Wang W L, Peng C Y, Chen W C, Liang M H, Tian J S and Chang L 2009 *Phys. Status Solidi (RRL)* **3** 109
[6] Vennéguès P, Chauveau J M, Korytov M, Deparis C, Zuniga-Perez J and Morhain C 2008 *J. Appl. Phys.* **103** 083525
[7] Wang W L, Peng C Y, Ho Y T, Chuang S C and Chang L 2011 *J. Vac. Sci. Technol.* A **29** 031001
[8] Schirra M, Schneider R, Reiser A, Prinz G M, Feneberg M, Biskupek J, Kaiser U, Krill C E, Thonke K and Sauer R 2008 *Phys. Rev.* B **77** 125215
[9] Romanov A E, Baker T J, Nakamura S and Speck J S 2006 *J. Appl. Phys.* **100** 023522
[10] Tian J S, Peng C Y, Wang W L, Wu Y H, Shih Y S, Chiu K A, Ho Y T, Chu Y H and Chang L 2013 *Phys. Status Solidi (RRL)* submitted
[11] Hayward S A *et al* 2005 *Phys. Rev.* B **72** 054110
[12] Harrison R J, Redfern S A T, Buckley A and Salje E K H 2004 *J. Appl. Phys.* **95** 1706
[13] Baker T J, Haskell B A, Wu F, Speck J S and Nakamura S 2006 *Japan. J. Appl. Phys.* **45** L154
[14] Narayan J and Larson B C 2003 *J. Appl. Phys.* **93** 278
[15] Young E C, Wu F, Romanov A E, Tyagi A, Gallinat C S, DenBaars S P, Nakamura S and Speck J S 2010 *Appl. Phys. Express* **3** 011004
[16] LeGoues F K, Reuter M C, Tersoff J, Hammar M and Tromp R M 1994 *Phys. Rev. Lett.* **73** 300
[17] Qian W, Skowronski M, Kaspi R, De Greaf M and Dravid V P 1997 *J. Appl. Phys.* **81** 7268
[18] Zúñiga-Pérez J, Muñoz-Sanjosé V, Palacios-Lidón E and Colchero J 2006 *Appl. Phys. Lett.* **88** 261912
[19] Wu F, Young E C, Koslow I, Hardy M T, Hsu P S, Romanov A E, Nakamura S, DenBaars S P and Speck J S 2011 *Appl. Phys. Lett.* **99** 251909
[20] Hardy M T, Hsu P S, Wu F, Koslow I L, Young E C, Nakamura S, Romanov A E, DenBaars S P and Speck J S 2012 *Appl. Phys. Lett.* **100** 202103
[21] Cherns D, Young W T, Sanders M, Steeds J W, Ponce F A and Nakamura S 1998 *Phil. Mag.* A **77** 273
[22] Northrup J E, Neugebauer J and Romano L T 1996 *Phys. Rev. Lett.* **77** 103
[23] Yan Y and Al-Jassim M M 2004 *Phys. Rev.* B **69** 085204
[24] Mclaurin M B, Hirai A, Young E C, Wu F and Speck J S 2008 *Japan. J. Appl. Phys.* **47** 5429
[25] Vennéguès P, Chauveau J M, Bougrioua Z, Zhu T, Martin D and Grandjean N 2012 *J. Appl. Phys.* **112** 113518
[26] Arroyo Rojas Dasilva Y, Chauvat M P, Ruterana P, Lahourcade L, Monroy E and Nataf G 2010 *J. Phys.: Condens. Matter* **22** 355802
[27] Vennéguès P, Bougrioua Z and Guehne T 2007 *Japan. J. Appl. Phys.* **46** 4089
[28] Vennéguès P, Mathal F and Bougrioua Z 2006 *Phys. Status Solidi* c **3** 1658
[29] Hirth J P and Lothe J 1982 *Theory of Dislocations* 2nd edn (New York: Wiley) p 91
[30] Speck J S, Brewer M A, Beltz G, Romanov A E and Pompe W 1996 *J. Appl. Phys.* **80** 3808
[31] Mathis S K, Romanov A E, Chen L F, Beltz G E, Pompe W and Speck J S 2001 *J. Cryst. Growth* **231** 371